PHYSICAL REVIEW B **102**, 224416 (2020)

# Orthorhombic $BiFeO_3$: Theoretical studies on magnetoelectric effects of the multiferroic phase

Ke Xu,[1,3,*] Guijie Liang,[1] Yu Feng,[4] H. J. Xiang,[3] and Junsheng Feng[2,3,†]

[1] *Hubei Key Laboratory of Low Dimensional Optoelectronic Materials and Devices, Hubei University of Arts and Science, Xiangyang, 441053, People's Republic of China*

[2] *School of Physics and Material Engineering, Hefei Normal University, Hefei 230601, People's Republic of China*

[3] *Key Laboratory of Computational Physical Sciences (Ministry of Education), State Key Laboratory of Surface Physics and Department of Physics, Fudan University, Shanghai 200438, People's Republic of China*

[4] *School of Physics and Electronic Engineering, Jiangsu Normal University, Xuzhou 221116, People's Republic of China*

(Received 29 January 2020; revised 8 September 2020; accepted 16 November 2020; published 15 December 2020)

The rhombohedral $BiFeO_3$ (BFO), as a star multiferroics, has been of particular interest, but yet it exhibits zero magnetization, which limits its practical application. Remarkably, net magnetization and magnetoelectric (ME) coupling was reported in orthorhombic BFO at room temperature in a recent experiment. However, the underlying mechanism of its ME coupling has not been fully understood. Here, we systematically investigated magnetic structures and ME coupling of the orthorhombic BFO using density functional theory and symmetry analysis. We find it can host large electric polarization and weak ferromagnetism simultaneously, the possible coupling between them is $\boldsymbol{\omega} \cdot (\boldsymbol{L} \times \boldsymbol{M})$. More interestingly, its polarization $P$ and magnetization $M$ can be switched simultaneously under an electric field, and it shows a linear ME effect when an external magnetic field is applied. Thus, our study provides a substantially deeper understanding of the ME effect of the orthorhombic BFO and confirm it is a multiferroic with the linear ME coupling.

DOI: 10.1103/PhysRevB.102.224416

## I. INTRODUCTION

Magnetoelectric (ME) multiferroics simultaneously possess polarization and magnetization, which has attracted more attention recently [1–7]. The coupling between the polarization and magnetization is a key ingredient to realize ME cross control. The ME coupling shows that the ME multiferroics not only have profound physics, but also have potential applications in multifunctional devices, such as low-power electronic devices and high-density memories [8,9]. The key factor to achieve ME cross control depends on the existence of ME coupling. Therefore, exploring the ME coupling effect has been an active topic in the field of multiferroics [10,11].

Up to now, it is well known that the celebrated room temperature multiferroic material is the rhombohedral [$R3c$ space group (SG)] $BiFeO_3$ (BFO), the ferroelectric transition temperature $T_C$ and magnetism transition temperature $T_N$ of which are 1100 and 640 K, respectively. Until now, tremendous progress on BFO has been made in both theories and experiments, such as weak Dzyaloshinskii-Moriya (DM) interactions and single ion anisotropy (SIA) [12–15], ME coupling [16–19], photovoltaic effect [20,21], spin dynamics and structural phase transitions [21]. Generally speaking, the ME coupling mainly focuses on the interaction between polarization $P$, magnetization $M$ and antiferromagnetic (AFM) order parameter $L$ [16–19]. Since the paraelectric phase of BFO has both inversion symmetry and time reversal symmetry, the ME coupling of the rhombohedral BFO may take the form of fourth-order coupling $P^2M^2$ and $P^2L^2$ [17].

In 2011, Diéguez *et al.* predicted that doped BFO might have a stable orthorhombic structure based on the first-principles calculations [22]. Since then, a recent experiment [23] indicated that the complex oxide $(1–x)BiTi_{(1–y)/2}Fe_yMg_{(1–y)/2}O_3–(x)CaTiO_3$ with the SG $Pna2_1$ is an ME multiferroics, the polarization and magnetization of which can be switchable. Moreover, a linear ME coupling effect at room temperature can be observed, when $x = 0.15$ and $y = 0.80$, suggesting that the polarization is tunable by an applied magnetic field [24]. Additionally, the phase transitions of the $R3c$ BFO also was studied by Raman spectroscopy [25], where a more stable orthorhombic $Pna2_1$ structure was reported with a weak ferromagnetism under a hydrostatic pressure of 3.5 GPa. As mentioned above, research has mainly focused on the structural stability, phase transitions, and magnetic structures of $R3c$ BFO. However, few studies on the orthorhombic phase of BFO have been reported so far. Especially, to our best knowledge, a systematic theoretical study about the magnetic order and (linear) ME coupling properties is still lacking. As we know, one main difference between $Pna2_1$ and $R3c$ phases is that the former one hosts the linear ME effect, while the latter one does not. The reason for that is the cycloidal magnetic structure in the $R3c$ one suppresses the linear ME effect [17]. Therefore, it is urgent to explore the ME coupling effect of the orthorhombic BFO, which cannot only deepen our understanding of the microscopic mechanism, but also provide theoretical guidance to design the ME cross control devices.

---

[*] xuke@hbuas.edu.cn

[†] fjs@hfnu.edu.cn

2469-9950/2020/102(22)/224416(7)

The paper is organized as follows. In Sec. II, we introduce the technical details of density functional theory (DFT) calculations. In Sec. III, the crystal structure of the orthorhombic BFO is presented and the corresponding polarization is calculated. In Sec. IV, the magnetic model and magnetic ground state of the orthorhombic BFO are provided. In Sec. V, we discuss the *P–L–M* coupling in orthorhombic BFO with the aid of magnetic group analysis. In Sec. VI, we study linear ME effect in the orthorhombic BFO. In Sec. VII, we summarize our results.

## II. METHODS AND CALCULATIONS

In this paper, the Vienna *ab initio* simulation package (VASP) [26,27] based on DFT [28] is used to optimize the geometrical structure and to calculate the electronic structure. The electronic wave function adopts the plane wave basis set, and the pseudopotential (PP) part adopts the projector augmented-wave scheme [29]. For Bi, Fe, and O, 15 valence electrons ($5d^{10}6s^26p^3$), 14 valence electrons ($2p^63d^64s^2$), and six valence electrons ($2s^22p^4$) PP are used, respectively. The exchange-correlation functional uses the generalized gradient approximation (GGA)–Perdew-Burke-Ernzerhof scheme [30]. For the $3d$ orbital of Fe, the GGA + U scheme [31] is used to treat the strong correlation properties of Fe's 3d electrons. The on-site Coulomb repulsion energy U and the Hund exchange parameter $J$ are set to 5.0 and 1.0 eV, respectively. The adopted U value is close to that adopted for $R3c$ BFO [19]. For lattice optimization, the energy cutoff is set to 550 eV to ensure the reliability of the stress tensor calculation during lattice relaxation; for structural relaxation, the force convergence criterion is that the Hellmann-Feynman force per atom is less than 0.001 eV/Å$^{-1}$. The Brillouin zone (BZ) is sampled using a Monkhorst-Pack scheme [32] with a $6 \times 6 \times 4$ $k$-point mesh for the BZ integration. The ferroelectric polarization is computed with the Berry phase method [33]; the magnetic field is implemented by introducing the Zeeman term [34] in VASP. The Heisenberg exchange interaction parameter $J$, DM interaction vector $D$, and SIA $A$ are obtained by the "four-state method" [35,36] within the framework of first-principles calculations. The phonon spectrum reflecting the structural dynamics stability is calculated with the PHONOPY [37] software package.

## III. BASIC STRUCTURE PROPERTIES AND MAGNETIC GROUND STATE OF BFO

The structure of the orthorhombic BFO with $Pna2_1$ SG is shown in Fig. 1(a). Each unit cell contains 20 atoms, i.e., four BFO formula units (f.u.). The Fe$^{3+}$ ions occupy the 4 $a$ Wyckoff position, so four Fe$^{3+}$ ions in the unit cell are symmetrically equivalent. The cubic $Pm\bar{3}m$ phase is deformed to the orthorhombic $Pna2_1$ phase, and the entire distortion process contains three steps. Firstly, two adjacent FeO$_6$ octahedrons are tilted along the [110] direction with antiphase rotation, the corresponding phonon mode is $R_5^-$. Secondly, the two adjacent FeO$_6$ octahedrons are tilted along the [001] direction with in-phase rotation, the corresponding phonon mode is $M_2^+$. At last, the Fe$^{3+}$ (B site) ions move along the [001] direction, and the phonon mode is $\Gamma_4^-$. The two rotation angles are different, so the entire distortion can be written as a compact Glazer symbol $a_0^-a_0^-c_+^+$ [38]. During this distortion, symmetry reduction is $Pm\bar{3}m \rightarrow Imma \rightarrow Pnma \rightarrow Pna2_1$. Note that the we use two sets of coordinate systems $\{abc\}$ and $\{xyz\}$ in Fig. 1 to represent the relationship between the lattice vector of orthorhombic phase and the cubic phase, namely $a = (x{-}y)/\sqrt{2}$, $b = (x + y)/\sqrt{2}$ and $c = z$. Unless otherwise stated, the global coordinate system $\{xyz\}$ is adopted in the text.

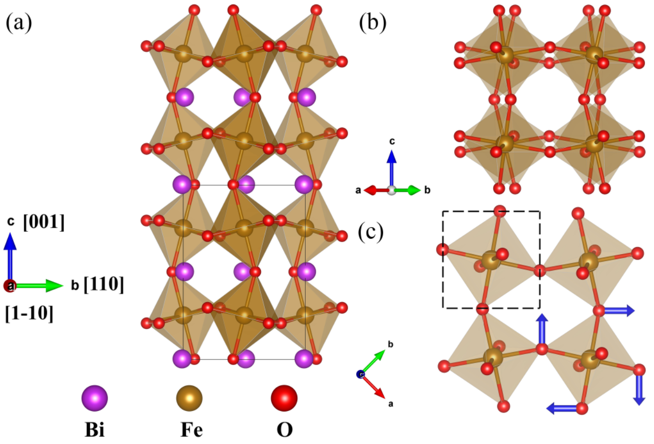

FIG. 1. (a) Structure of the orthorhombic $Pna2_1$ BFO; (b) Side view of the Fe–O octahedron rotation. The in-plane two octahedrons have out-of-phase rotation; (c) Side view of the Fe–O octahedral rotation. The out-of-plane two octahedral have in phase rotation. The dashed square denotes the unit cell of the $Pm\bar{3}m$ parent structure.

The geometrical structure and lattice constant of four typical magnetic configurations, i.e., A–type, C–type, G–type AFM state and F–type ferromagnetic (FM) state, are optimized by the DFT + U scheme. The calculation results show that the $Pna2_1$ BFO prefers the G–type AFM configuration, since the other three magnetic configurations of A–type, C–type, and FM have 128.06, 53.53, and 200.05 meV/f.u. higher energies than the G–type AFM. In our calculation, the lattice constants are 5.699, 5.511, and 8.064 Å, respectively. In particular, the average bond angle of Fe–O–Fe, average bond length Fe–O and the energy difference between the two magnetic states (FM and G–AFM) are 150.94°, 2.06 Å, and 200.05 meV/f.u., which is very close to Diéguez's results (150°, 2.13 Å, and 200 meV/f.u.) [22]. If U = 5 eV and $J = 1$ eV are adopted, the band gap is predicted to be 2.0 eV. The polarization is computed to be 41.40 $\mu$C/cm$^2$ along the $z$ direction, which is also consistent with the experimental value [39]. In order to discuss the stability of $Pna2_1$ BFO, we compute the energy of the rhombohedral phase and the orthorhombic phase under different pressure. Under ambient pressure, the $R3c$ phase has a 46 meV/f.u. energy lower than that of $Pna2_1$ phase. As the hydrostatic pressure increases, $Pna2_1$ phase gradually becomes the ground state at 4.2 GPa, see Fig. 2(a), which is close to the experimental value of 3.5 GPa [25]. On the other hand, as shown in Fig. 2(b), phonon dispersions without imaginary frequencies indicate that $Pna2_1$ BFO is dynamically stable. Our results show that phase transition from $R3c$ to $Pna2_1$ takes place under high pressure and the orthorhombic phase is stable under ambient

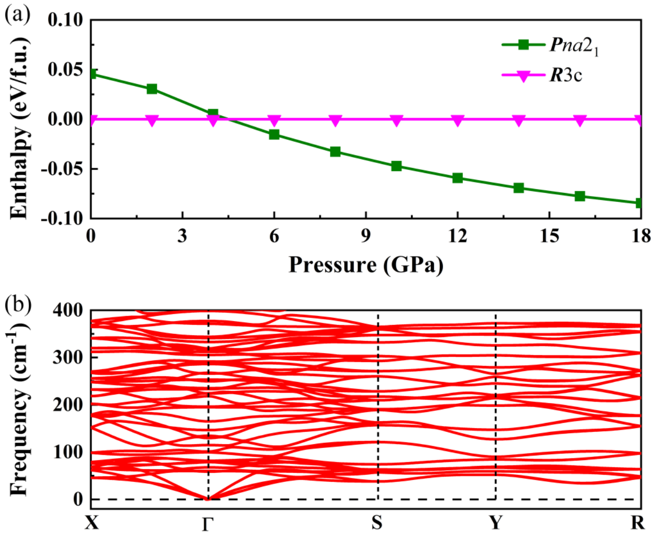

FIG. 2. (a) The evolution of enthalpy as the function of hydrostatic pressure for two different BFO phases. (b) Phonon dispersion of BFO for the *Pna*2$_1$ phase. There are no imaginary frequencies indicating that the *Pna*2$_1$ structure is stable. The phonon dispersion is calculated using the PHONOPY code based on a supercell approach, where the force constants are obtained by GGA + U calculations.

pressure, ensuring that *Pna*2$_1$ BFO has potential application in spintronics.

## IV. MAGNETIC PROPERTIES OF BFO

To further study the magnetic interaction in *Pna*2$_1$ BFO, the four-state method is used to calculate the effective Heisenberg exchange constant $J$ and DM interaction vector $D$. Since the magnetic interaction is short-range, only Fe–Fe ion pairs with a distance less than 6 Å are considered. The symmetry of orthorhombic phase is much lower than that of the cubic phase, so the originally degenerate interaction paths in the cubic structure split. There are nine inequivalent Fe–Fe exchange interaction paths in *Pna*2$_1$ BFO. The first three paths are nearest neighbors (NN) shown in Fig. 3(a). The Fe–Fe ion pair sharing an oxygen anion forms a Fe–O–Fe super exchange interaction pathway; the remaining six pairs are next nearest neighbors (NNN), corresponding to the Fe–O⋯O–Fe super-super exchange pathway shown in Fig. 3(b). The calculated results show that all exchange interactions are AFM, and the NN pairs have the largest exchange parameter ($J_{\text{NN}} > 34$ meV). The exchange parameters $J$s, Fe–O bond lengths, and the Fe–O–Fe bond angles are listed in Table I. The magnitude and sign of the superexchange interaction are consistent with the Goodenough-Kanamori-Anderson rule [40,41], i.e., the shorter the bond length, the closer the bond angle is to 180° (about 150°), the stronger AFM. Since the NNN pairs have relatively weak AFM interactions ($J_{\text{NNN}} < 2$ meV), far less than the NN pairs interaction, we may neglect them. Therefore, the magnetic moments (MM) of the NN pair are arranged in antiparallel manner, the system has the lowest energy. This checkboard alignment is dubbed as the collinear G–type AFM.

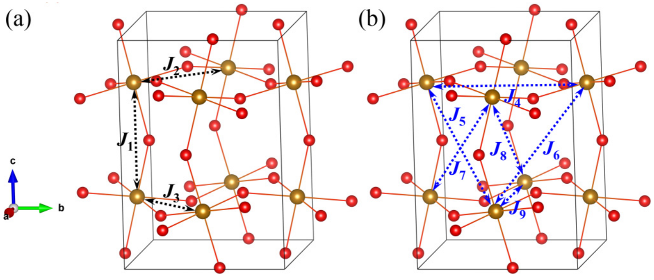

FIG. 3. Spin exchange interactions in BFO. (a) The nearest neighbor superexchange paths; (b) The next nearest neighbor super-superexchange paths.

TABLE I. The nearest-neighbor Heisenberg interaction parameters.

| $J_{\text{NN}}$ | dFe–Fe (Å) | dFe$_1$–O(Å) | dFe$_2$–O(Å) | ∠Fe–O–Fe (°) | $J_{\text{eff}}$ (meV) |
|---|---|---|---|---|---|
| 1 | 3.963 | 2.013 | 2.047 | 150.76 | 37.123 |
| 2 | 3.965 | 2.038 | 2.077 | 148.89 | 35.544 |
| 3 | 4.032 | 2.148 | 1.997 | 153.18 | 33.658 |

The magnetic anisotropy calculation demonstrates that the MM along the $y$ direction has the lowest energy (i.e., 0.75 and 0.50 meV lower than the MM along the $x$ and $z$ directions, respectively). The spin-orbit coupling (SOC) calculation manifests that *Pna*2$_1$ BFO is a weak FM with a 0.100 $\mu_{\text{B}}$ MM along the $z$ direction. This weak (or canting) ferromagnetism originates from DM interactions [42,43]. To identify the ground state magnetic structure of BFO, Monte Carlo (MC) simulation is carried out at low temperature (∼3 K) based on the following magnetic Hamiltonian:

$$\hat{H}_{\text{spin}} = \sum_{\langle ij\rangle,\langle\langle ij\rangle\rangle} J_{ij}\hat{S}_i\cdot\hat{S}_j + \sum_{\langle ij\rangle}\boldsymbol{D}_{ij}\cdot\left(\hat{S}_i\times\hat{S}_j\right) + A_{yy}\sum_i\left(\hat{S}_i^y\right)^2, \tag{1}$$

where $\langle ij\rangle/\langle\langle ij\rangle\rangle$ denotes the NN/NNN interactions and $A_{yy}$ ($-0.19$ meV) is the single ion anisotropy. The MC simulation shows that at low temperature the MMs along the $y$ direction adopt the G–type AFM (G$_y$) with large magnitude, the MMs along the $x$ direction form the A–type AFM (A$_x$) and the MMs along $z$ direction form F–type weak FM (F$_z$), respectively. The net MM is about 0.160 $\mu_{\text{B}}$, along the $z$ direction, which is completely consistent with the DFT + U + SOC calculation. Therefore, the *Pna*2$_1$ BFO displays weak ferromagnetism.

## V. MAGNETIC GROUP ANALYSIS AND COUPLING BETWEEN POLARIZATION AND MAGNETISM

The magnetic symmetry of aforementioned four magnetic structures (FM, A–AFM, C–AFM, G–AFM) are different in *Pna*2$_1$ BFO. We use the group theory method to classify the irreducible representations (IRs) of the four magnetic orders. The point group of the *Pna*2$_1$ SG is $C_{2v}$, which has four IRs. Therefore, the *Pna*2$_1$ has four possible magnetic SG (*Pna*2$_1$, *Pn'a'*2$_1$, *Pn'a*2$_1'$, *Pna'*2$_1'$). Since four Fe$^{3+}$ ions are equivalent through the symmetry operation, we may choose one of four Fe$^{3+}$ ion (we label it as “1”) to perform the projection operation [see Eq. (2)], it is easy to identify the magnetic SG

TABLE II. The nonzero linear magnetoelectric tensor associate with magnetic order and magnetic point group.

| IR | 1 | $2_1[001]$ | n[001] | a[010] | Magnetic orders | Magnetic point group(SG) | Linear ME tensor |
|---|---|---|---|---|---|---|---|
| $A_1$ | 1 | 1 | 1 | 1 | $G_xA_yC_z$ | $mm2$ ($Pna2_1$) | $\alpha_{xy}$,$\alpha_{yx}$ |
| $A_2$ | 1 | 1 | −1 | −1 | $A_xG_yF_z$ | $m'm'2$ ($Pn'a'2_1$) | $\alpha_{xx}$,$\alpha_{yy}$, $\alpha_{zz}$ |
| $B_1$ | 1 | −1 | −1 | 1 | $C_xF_yG_z$ | $m'm2'$($Pn'a2_1{}'$) | $\alpha_{yz}$,$\alpha_{zy}$ |
| $B_2$ | 1 | −1 | 1 | −1 | $F_xC_yA_z$ | $mm'2'$($Pna'2_1{}'$) | $\alpha_{xz}$,$\alpha_{zx}$ |

corresponding to four possible magnetic orders:

$$\hat{P}^{\Gamma_i} M_{1,\alpha} \sim \sum_{j=1}^{4} \chi_j^{\Gamma_i}(\hat{R}_j) M_{1,\alpha}, \tag{2}$$

where $\Gamma_\text{i}$ is the $i$th IR of the $C_{2v}$ point group, $\chi_j^{\Gamma_i}(\hat{R}_j)$ is the character of the $j$th symmetric operation of the $i$th IR and $M_{1,\alpha}$ represents spin magnetic moment along the $\alpha$ direction ($\alpha = x, y, z$). In our calculation, the ground state of BFO has $G_y$ magnetic order, which belongs to the $A_2$ IR, therefore the corresponding magnetic SG is $Pn'a'2_1$. Here, $\hat{R}'$ is the joint symmetry operator $\hat{T}\hat{R}$ ($\hat{T}$ is time reversal operation). Interestingly, $A_x$ and $F_z$ magnetic orders also belong to the $A_2$ IR, indicating that the ground state of BFO may exhibit a weak ferromagnetism in the $z$ direction. The IRs of four magnetic orders are list in Table II.

After discussing the magnetic symmetry, we now explore the coupling between polarization and magnetism in $Pna2_1$ BFO. With symmetry analysis, we find that there are 12 domains for $Pna2_1$ BFO. Here we consider four domains with polarization along $z$ or $-z$ directions. We define the FM order parameter $M = M_1 + M_2 + M_3 + M_4$ and the AFM order parameter $L = M_1 - M_2 - M_3 + M_4$, where $M_i$ is the MM of the $i$th $\text{Fe}^{3+}$ ion in the unit cell. Its geometry, ferroelectric mode $\Gamma_4^-$, rotation mode $R_5^-$, tilt mode $M_2^+$, $X_5^+$ mode, AFM order parameter $L$, and FM order parameter $M$ are shown in Figs. 4(a), 4(b), 4(c), and 4(d), respectively. For each ferroelectric domain, the FM order $M$ is always parallel or antiparallel to the polarization $P$, while the AFM order $L$ is always perpendicular to the polarization $P$. For a perovskite, one possible ME coupling mechanism is $\boldsymbol{\omega} \cdot (\boldsymbol{L} \times \boldsymbol{M})$ as proposed by Bellaiche *et al.* [44,45], where $\boldsymbol{\omega}$ is the direction of $R_5^-$ mode. This suggests that if one reverses the $R_5^-$ mode (e.g., from clockwise to anticlockwise) and keeps the AFM order parameter $L$ invariant, the FM order parameter $M$ will be reversed (note that changing $M$ is easier than changing $L$ as the canting ferromagnetic moment is small). The reversal of the $R_5^-$ mode may be associated with the reversal of the $\Gamma_4^-$ FE mode, as can be seen from Figs. 4(a) and 4(b). This is consistent with the quadralinear coupling [see Fig. 4(e)] in the $Pna2_1$ perovskite system first pointed out by Lou *et al.* [45]. Therefore, the $\boldsymbol{\omega} \cdot (\boldsymbol{L} \times \boldsymbol{M})$ and the quadralinear coupling might result in the reversal of the ferromagnetism by an electric field. The schematic diagram of this ME coupling is shown in Fig. 4(f). The domain I ($P//c$, $L//b$, $\omega//-a$, and $M//c$) has the same energy as the domain II ($P//-c$, $L//b$, $\omega//a$, and $M//-c$). Since $P$ and $M$ may be flipped simultaneously in $Pna2_1$ BFO, this 180° flip brings the convenience of practical application, which is completely different from $R3c$, e.g., 71° or 109° magnetization switching [46].

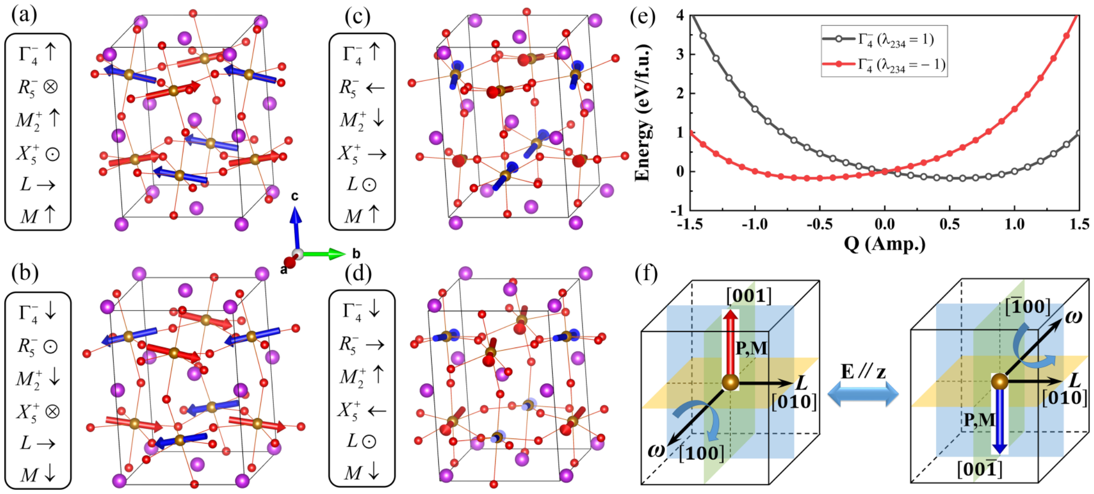

FIG. 4. (a), (b), (c), and (d) Magnetic structures of the four nonequivalence domains of BFO with the polarization along $c$ or $-c$. The directions of the structural phonon modes $\Gamma_4^-$, $R_5^-$, $M_2^+$ and $X_5^+$, antiferromagnetic order parameter $L$ and ferromagnetic order $M$ are indicated for these domains, where ↑ (↓) represents the $c$($-c$) direction, → (←) represents the $b$($-b$) direction, and ⊙ (⊗) represents the $a$($-a$) direction. (e) The quadralinear coupling between the FE mode and the other three normal modes. $\lambda_{234} = \pm 1$ depicts $Q(R_5^-) = \pm 1$, $Q(M_2^+) = \pm 1$, and $Q(X_5^+) = \pm 1$, and illustration of the ME coupling in BFO. As an example, we show a possible 180° switching of the ferroelectric domains of the BFO by the external electric field associated with the reorientation of the magnetization.

## VI. LINEAR ME EFFECT IN BFO

ME multiferroic materials have potential applications in magnetic field detectors, such as electrically switchable permanent magnets, magnetic memory, and magneto-optical devices, as well as wireless energy transfer and energy saving technologies [47], in which linear ME coupling is the key point. Note that the linear ME effect to be discussed in this part is different from the ME effect discussed in the previous part as the electric field is so large that the electric polarization is switched in the latter case. When the external fields are applied, the free energy $F$ is the coupling between the electric field $E$ and the magnetic field $H$ in $Pna2_1$ BFO [24]:

$$F(\boldsymbol{E},\boldsymbol{H}) = -P_i^S E_i - M_i^S H_i - \frac{1}{2}\varepsilon_0\varepsilon_{ij}E_iE_j - \frac{1}{2}\mu_0\mu_{ij}H_iH_j - \boldsymbol{\alpha}_{ij}\boldsymbol{E}_i\boldsymbol{H}_j - \frac{1}{2}\beta_{ijk}E_iH_jH_k - \frac{1}{2}\gamma_{ijk}H_iE_jE_k + \cdots . \qquad (3)$$

Differentiating the free energy $F$ with respect to the magnetic field $H$ or the electric field $E$, one obtains the induced electric polarization $P$ or magnetization $M$, proportional to the applied magnetic field $H$ or electric field $E$, which can be expressed as $P = \alpha H$ or $M = \alpha E$, and the linear ME coupling coefficient $\alpha$ is the second rank tensor. Since the electric field $E$ and the magnetic field $H$ change their sign under the spatial inversion $\hat{I}$ and the time reversal $\hat{T}$, respectively, the linear ME coupling tensor $\alpha$ must maintain invariant under the compound transformation of time reversal and spatial inversion. The nonzero components of tensor $\alpha$ is related to the magnetic orders and the IR of the point group [48]. According to Neumann's principle [49], the linear ME component $\alpha_{ij}$ under symmetric operation $\hat{R}$ is $\alpha_{ij} = |\hat{R}|\theta R_{il}R_{jm}\alpha_{lm}$, where $|\hat{R}| = 1$ or $-1$ for proper or improper rotations and $\theta = 1$ or $-1$ for absence or presence of time reversal. For orthorhombic phase BFO, the linear ME coupling tensor $\alpha$ can be further simplified under the $Pn'a'2_1$ magnetic SG, and the nonzero components are listed in Table II. For the A$_x$, G$_y$, and F$_z$ magnetic orders, the linear ME coupling free energy $F_{LME}$ has a simple form:

$$F_{LME} = -\alpha_{xx}E_xH_x - \alpha_{yy}E_yH_y - \alpha_{zz}E_zH_z. \qquad (4)$$

Equation (4) shows that the $i$ direction ($i = x, y, z$) magnetic field induces the polarization along the $i$ direction. The group theory method can only determine the nonzero element of the linear ME tensor (i.e., $\alpha_{xx}$, $\alpha_{yy}$ and $\alpha_{zz}$) but not the magnitude of the nonzero components. Since the net canting MM of orthorhombic phase BFO along the $z$ direction is small, when the applied magnetic field is in the $y$ direction, the generated spin torque is also small and can be neglected. That is to say, the $y$ direction magnetic field only hardly changes the electron density and induces the $y$ direction polarization, therefore $\alpha_{yy}$ is approximated to be zero. Based on above analysis, we only need to calculate $\alpha_{xx}$ and $\alpha_{zz}$. Hence, the ME coupling tensor $\alpha$ originates from the deformation of the electronic cloud and ions displacement, i.e., $\alpha^{\text{tot}} = \alpha^{el} + \alpha^{latt}$ for $xx$ and $zz$ components. We first calculate the electronic ME contribution with frozen ions. To compute the changes in the ionic polarizations, ionic relaxation is performed in the presence of external magnetic fields. The forces induced by external magnetic field are very small, therefore, very rigorous convergence criterions of the energy and ionic forces are needed. The energy and ionic forces are reduced to $10^{-10}$ eV and $10^{-7}$ eV/Å with respect to a much larger plane wave cutoff energy (700 eV) in our calculations. The change in the polarization is defined as $\Delta P(H) = P(H) - P(0)$, where $P(H)$ is the polarization in the presence of magnetic field and $P(0)$ is the polarization at zero field, and the electric and ions polarization are calculated by the Berry phase approach [33]. When the magnetic field is along the $x$ axis, the polarization changes are shown as open square, open circles and circles for electronic, ionic, and total, respectively, in Figs. 5(a) and 5(b). From Fig. 5(a), we see that the ME response contains linear and nonlinear components [50] and the linear components dominate. The calculated $\alpha_{xx}^{el}$ and $\alpha_{xx}^{latt}$ are $-0.32$ and $-2.27$ ps/m, respectively. When the magnetic field is along the $z$ axis, the calculated $\alpha_{zz}^{latt}$ is 3.37 ps/m and Fig. 5(b) shows that $\alpha_{zz}^{el}$ is much smaller than that of $\alpha_{zz}^{latt}$. Therefore, $\alpha_{zz}^{el}$ can be ignored here. Our results show that the $|\alpha_{xx}^{\text{tot}}|$ and $\alpha_{zz}^{\text{tot}}$ of BFO are both larger than that of Cr$_2$O$_3$ ($\alpha_{\perp}^{\text{tot}} = 1.45$ ps/m) [34].

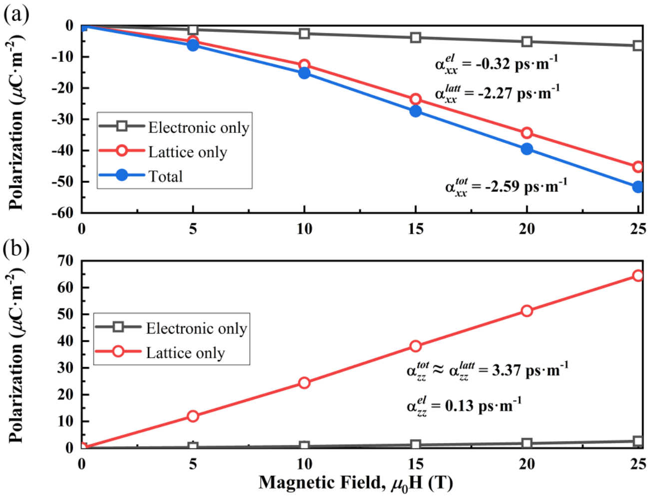

FIG. 5. The change in the polarization of the BFO as a function of the magnetic field. (a) The electronic and ionic polarizations when the magnetic field is along the $x$ axis. (b) The electronic and ionic polarizations when the magnetic field is parallel to the $z$ axis.

At last, we compare the linear ME coupling coefficients of rhombohedral and tetragonal BFO with that of orthorhombic BFO. In the absence of incommensurate spin modulation, the rhombohedral phase exhibits a smaller linear ME response ($\alpha = 1.67$ ps/m) [51] than the orthorhombic phase ($\alpha_{xx} = 2.59$ ps/m), while the tetragonal phase has a larger ME response ($\alpha > 5$ ps/m) [52] than the orthorhombic phase ($\alpha_{zz} = 3.37$ ps/m).

## VII. CONCLUSIONS

The DFT calculations show that the orthorhombic BFO has the same order of polarization as the rhombohedral phase and has a small net magnetic moment, which provides a prerequisite for the application of the orthorhombic BFO as an applicable multiferroic material. Landau free energy, domain, symmetry analysis show that *P* and *M* in $Pna2_1$ BFO may be flipped simultaneously. This possible ME coupling mechanism indicates that when the polarization is reversed from $z$ to $-z$, the magnetization may also be reversed by 180°. The symmetry analysis shows that the linear ME tensor of the orthorhombic BFO has a diagonal form, and the polarization can be induced by applied magnetic field in the $x$ and $z$ directions. Hence, the orthorhombic BFO is a magnetoelectric multiferroic material that can directly realize the cross controlling of magnetoelectricity under room temperature.

## ACKNOWLEDGMENTS

This work was supported by NSFC (Grant No. 11404109), Hubei Provincial Natural Science Foundation (Grant No. 2019CFB774), and supported by Anhui Provincial Natural Science Foundation (Grant No. 1908085MA10). We thank Dr. F. Lou for useful discussions. Special thanks to Prof. N. A. Spaldin of ETH Zurich and Dr. E. Bousquet of the University of Liège for providing us the modified VASP subroutines that implemented the Zeeman term.

[1] N. A. Spaldin and M. Fiebig, The renaissance of magnetoelectric multiferroics, Science **309**, 391 (2005).

[2] S. W. Cheong and M. Mostovoy, Multiferroics: A magnetic twist for ferroelectricity, Nat. Mater. **6**, 13 (2007).

[3] R. Ramesh and N. A. Spaldin, Multiferroics: Progress and prospects in thin films, Nat. Mater. **6**, 21 (2007).

[4] K. F. Wang, J. M. Liu, and Z. F. Ren, Multiferroicity: The coupling between magnetic and polarization orders, Adv. Phys. **58**, 321 (2009).

[5] Y. Tokura and S. Seki, Multiferroics with spiral spin orders, Adv. Mater. **22**, 1554 (2010).

[6] P. S. Wang, X. Z. Lu, X. G. Gong, and H. J. Xiang, Microscopic mechanism of spin-order induced improper ferroelectric polarization, Comput. Mater. Sci. **112**, 448 (2016).

[7] S. Dong, H. J. Xiang, and E. Dagotto, Magnetoelectricity in multiferroics: A theoretical perspective, Natl. Sci. Rev. **6**, 629 (2019).

[8] S. Manipatruni, D. E. Nikonov, C. C. Lin, B. Prasad, Y. L. Huang, A. R. Damodaran, Z. H. Chen, R. Ramesh, and I. A. Young, Voltage control of unidirectional anisotropy in ferromagnet-multiferroic system, Sci. Adv. **4**, eaat4229 (2018).

[9] J. F. Scott, Data storage: Multiferroic memories, Nat. Mater. **6**, 256 (2007).

[10] P. S. Wang, W. Ren, L. Bellaiche, and H. J. Xiang, Predicting a Ferrimagnetic Phase of $Zn_2FeOsO_6$ with Strong Magnetoelectric Coupling, Phys. Rev. Lett. **114**, 147204 (2015).

[11] J. S. Feng, K. Xu, L. Bellaiche, and H. J. Xiang, Designing switchable near room-temperature multiferroics via the discovery of a novel magnetoelectric coupling, New J. Phys. **20**, 053025 (2018).

[12] R. S. Fishman, Field dependence of the spin state and spectroscopic modes of multiferroic $BiFeO_3$, Phys. Rev. B **87**, 224419 (2013).

[13] U. Nagel, R. S. Fishman, T. Katuwal, H. Engelkamp, D. Talbayev, H. T. Yi, S. W. Cheong, and T. Rõõm, Terahertz Spectroscopy of Spin Waves in Multiferroic $BiFeO_3$ in High Magnetic Fields, Phys. Rev. Lett. **110**, 257201 (2013).

[14] R. S. Fishman, J. T. Haraldsen, N. Furukawa, and S. Miyahara, Spin state and spectroscopic modes of multiferroic $BiFeO_3$, Phys. Rev. B **87**, 134416 (2013).

[15] R. S. Fishman, J. H. Lee, S. Bordács, I. Kézsmárki, U. Nagel, and T. Rõõm, Spin-induced polarizations and nonreciprocal directional dichroism of the room-temperature multiferroic $BiFeO_3$, Phys. Rev. B **92**, 094422 (2015).

[16] M. Ramazanoglu, M. Laver, W. Ratcliff, S. M. Watson, W. C. Chen, A. Jackson, K. Kothapalli, S. Lee, S. W. Cheong, and V. Kiryukhin, Local Weak Ferromagnetism in Single-Crystalline Ferroelectric $BiFeO_3$, Phys. Rev. Lett. **107**, 207206 (2011).

[17] X. X. Shi, X. Q. Liu, and X. M. Chen, Readdressing of magnetoelectric effect in bulk $BiFeO_3$, Adv. Funct. Mater. **27**, 1604037 (2017).

[18] M. Mostovoy, Ferroelectricity in Spiral Magnets, Phys. Rev. Lett. **96**, 067601 (2006).

[19] Y. K. Weng, L. F. Lin, E. Dagotto, and S. Dong, Inversion of Ferrimagnetic Magnetization by Ferroelectric Switching Via a Novel Magnetoelectric Coupling, Phys. Rev. Lett. **117**, 037601 (2016).

[20] T. Choi, S. Lee S, Y. J. Choi, and S. W. Cheong, Switchable ferroelectric diode and photovoltaic effect in $BiFeO_3$, Science **324**, 63 (2009).

[21] I. Kézsmárki, U. Nagel, S. Bordács, R. S. Fishman, J. H. Lee, H. T. Yi, S. W. Cheong, and T. Rõõm, Optical Diode Effect at Spin-Wave Excitations of the Room-Temperature Multiferroic $BiFeO_3$, Phys. Rev. Lett. **115**, 127203 (2015).

[22] O. Diéguez, O. E. Gonzáez-Vázquez, J. C. Wojdeł, and J. Íñiguez, First-principles predictions of low-energy phases of multiferroic $BiFeO_3$, Phys. Rev. B **83**, 094105 (2011).

[23] P. Mandal, M. J. Pitcher, J. Alaria, H. Niu, P. Borisov, P. Stamenov, J. B. Claridge, and M. J. Rosseinsky, Designing switchable polarization and magnetization at room temperature in an oxide, Nature (London) **525**, 363 (2015).

[24] M. Fiebig, Revival of the magnetoelectric effect, J. Phys. D **38**, R123 (2005).

[25] J. Buhot, C. Toulouse, Y. Gallais, A. Sacuto, R. de Sousa, D. Wang, L. Bellaiche, M. Bibes, A. Barthélémy, A. Forget, D. Colson, M. Cazayous, and M. A. Measson, Driving Spin Excitations by Hydrostatic Pressure in $BiFeO_3$, Phys. Rev. Lett. **115**, 267204 (2015).

[26] G. Kresse and J. Hafner, *Ab initio* molecular dynamics for liquid metals, Phys. Rev. B **47**, 558(R) (1993).

[27] G. Kresse and J. Furthmuller, Efficiency of ab initio total energy calculations for metals and semiconductors using a plane-wave basis set, Comput. Mater. Sci. **6**, 15 (1996).

[28] P. Hohenberg and W. Kohn, Inhomogeneous electron gas, Phys. Rev. **136**, B864 (1964).

[29] P. E. Blöchl, Projector augmented-wave method, Phys Rev. B **50**, 17953 (1994).

[30] J. P. Perdew, K. Burke, and M. Ernzerhof. Generalized Gradient Approximation Made Simple, Phys. Rev. Lett. **77**, 3865 (1996).

[31] V. I. Anisimov, F. Aryasetiawan, and A. I. Lichtenstein, First-principles calculations of the electronic structure and spectra

of strongly correlated systems: the LDA+ U method, J. Phys.: Condens. Matter **9**, 767 (1997).

[32] H. J. Monkhorst and J. D. Pack, Special points for Brillouin-zone integrations, Phys. Rev. B **13**, 5188 (1976).

[33] R. Resta, Macroscopic polarization in crystalline dielectrics: The geometric phase approach, Rev. Mod. Phys. **66**, 899 (1994).

[34] E. Bousquet, N. A. Spaldin, and K. T. Delaney, Unexpectedly Large Electronic Contribution to Linear Magnetoelectricity, Phys. Rev. Lett. **106**, 107202 (2011).

[35] H. J. Xiang, E. J. Kan, Su-Huai Wei, M.-H. Whangbo, and X. G. Gong, Predicting the spin-lattice order of frustrated systems from first principles, Phys. Rev. B **84**, 224429 (2011).

[36] H. J. Xiang, C. H. Lee, H. J. Koo, X. G. Gong, and M. H. Whangbo, Magnetic properties and energy-mapping analysis, Dalton Trans. **42**, 823 (2013).

[37] A. Togo, F. Oba, and I. Tanaka, First-principles calculations of the ferroelastic transition between rutile-type and $\mathrm{CaCl_2}$-type $\mathrm{SiO_2}$ at high pressures, Phys Rev B **78**, 134106 (2008).

[38] H. T. Stokes, E. H. Kisi, D. M. Hatch, and C. J. Howard, Group-theoretical analysis of octahedral tilting in ferroelectric perovskites, Acta Cryst. B, **58**, 934 (2002).

[39] W. R. Geng, X. W. Guo, Y. L. Zhu, Y. L. Tang, Y. P. Feng, M. J. Zou, Y. J. Wang, M. J. Han, J. Y. Ma, B. Wu, W. T. Hu, and X. L. Ma, Rhombohedral-orthorhombic ferroelectric morphotropic phase boundary associated with a polar vortex in $\mathrm{BiFeO_3}$ films, ACS Nano **12**, 11098 (2018).

[40] I. Dzyaloshinsky, A thermodynamic theory of "weak" ferromagnetism of antiferromagnetics, J. Phys. Chem. Solids **4**, 241 (1958).

[41] T. Moriya, Anisotropic superexchange interaction and weak ferromagnetism, Phys. Rev. **120**, 91 (1960).

[42] J. B. Goodenough, Theory of the role of covalence in the perovskite-type manganites [La, M(II)]$\mathrm{MnO_3}$, Phys. Rev. **100**, 564 (1955).

[43] J. Kanamori, Superexchange interaction and symmetry properties of electron orbitals, J. Phys. Chem. Solids. **10**, 87 (1959).

[44] L. Bellaiche, Z. G. Gui, and I. A. Kornev, A simple law governing coupled magnetic orders in perovskites, J. Phys.: Condens. Matter **24**, 312201 (2012).

[45] F. Lou, W. Luo, J. S. Feng, and H. J. Xiang, Genetic algorithm prediction of pressure-induced multiferroicity in the perovskite $\mathrm{PbCoO_3}$, Phys. Rev. B **99**, 205104 (2019).

[46] J. T. Heron, J. L. Bosse, Q. He, Y. Gao, M. Trassin, L. Ye, J. D. Clarkson, C. Wang, Jian Liu, S. Salahuddin, D. C. Ralph, D. G. Schlom, J. Íñiguez, B. D. Huey, and R. Ramesh, Deterministic switching of ferromagnetism at room temperature using an electric field, Nature **516**, 370 (2014).

[47] A. P. Pyatakov and A. K. Zvezdin, Magnetoelectric and multiferroic media, Phys. Usp. **55**, 557 (2012).

[48] E. Bousquet and E. Spaldin, Induced Magnetoelectric Response in *Pnma* Perovskites, Phys. Rev. Lett. **107**, 197603 (2011).

[49] M. El-Batanouny and F. Wooten, *Symmetry and Condensed Matter Physics A Computational Approach* (Cambridge University Press, Cambridge, 2008), pp. 474–475.

[50] A. C. Garcia-Castro, A. H. Romero, and E. Bousquet, Strain-Engineered Multiferroicity in *Pnma* $\mathrm{NaMnF_3}$ Fluoroperovskite. Phys. Rev. Lett. **116**, 117202 (2016).

[51] J. C. Wojdeł and J. Íñiguez, Magnetoelectric Response of Multiferroic $\mathrm{BiFeO_3}$ and Related Materials from First-Principles Calculations, Phys. Rev. Lett. **103**, 267205 (2009).

[52] J. C. Wojdeł and J. Íñiguez, *Ab initio* Indications for Giant Magnetoelectric Effects Driven by Structural Softness, Phys. Rev. Lett. **105**, 037208 (2010).